



# Yet Another Sunshine Mystery: Unexpected Asymmetry in GeV Emission from the Solar Disk

Bruno Arsioli<sup>1,2,3,4</sup>  and Elena Orlando<sup>3,4,5</sup><sup>1</sup> Institute of Astrophysics and Space Science, OAL, University of Lisbon, Tapada da Ajuda, 1349-018 Lisbon, Portugal; [bruno.arsioli@gmail.com](mailto:bruno.arsioli@gmail.com)<sup>2</sup> Department of Physics, Faculty of Sciences, University of Lisbon, Edifício C8, Campo Grande, 1749-016 Lisbon, Portugal<sup>3</sup> University of Trieste, Department of Physics Via Valerio 2, 34127 Trieste, Italy; [orland.ele@gmail.com](mailto:orland.ele@gmail.com)<sup>4</sup> Istituto Nazionale di Fisica Nucleare—INFN Padriciano, 99, I-34149 Trieste, Italy<sup>5</sup> Stanford University, Stanford, CA 94305, USA

Received 2023 October 11; revised 2023 December 22; accepted 2024 January 4; published 2024 February 7

## Abstract

The Sun is one of the most luminous  $\gamma$ -ray sources in the sky and continues to challenge our understanding of its high-energy emission mechanisms. This study provides an in-depth investigation of the solar disk  $\gamma$ -ray emission, using data from the Fermi Large Area Telescope spanning 2008 August to 2022 January. We focus on  $\gamma$ -ray events with energies exceeding 5 GeV, originating from 0.5° angular aperture centered on the Sun, and implement stringent time cuts to minimize potential sample contaminants. We use a helioprojection method to resolve the  $\gamma$ -ray events relative to the solar rotation axes and combine statistical tests to investigate the distribution of events over the solar disk. We found that integrating observations over large time windows may overlook relevant asymmetrical features, which we reveal in this work through a refined time-dependent morphological analysis. We describe significant anisotropic trends and confirm compelling evidence of energy-dependent asymmetry in the solar disk  $\gamma$ -ray emission. Intriguingly, the asymmetric signature coincides with the Sun's polar field flip during the cycle 24 solar maximum, around 2014 June. Our findings suggest that the Sun's magnetic configuration plays a significant role in shaping the resulting  $\gamma$ -ray signature, highlighting a potential link between the observed anisotropies, solar cycle, and the solar magnetic fields. These insights pose substantial challenges to established emission models, prompting fresh perspectives on high-energy solar astrophysics.

*Unified Astronomy Thesaurus concepts:* [Quiet sun \(1322\)](#); [Solar gamma-ray emission \(1497\)](#); [Solar cycle \(1487\)](#); [Solar magnetic fields \(1503\)](#); [High energy astrophysics \(739\)](#)

*Supporting material:* animations

## 1. Introduction

The Sun, a persistent and intense source of  $\gamma$ -ray emission, manifests a plethora of processes within its solar atmosphere. Efforts to model and quantify the solar  $\gamma$ -ray flux date back to Seckel et al. (1991), a time when detecting the solar disk's  $\gamma$ -ray signature was thought to be within the capabilities of forthcoming detectors like the EGRET on board the Compton Gamma Ray Observatory (Gehrels et al. 1993). Since then, one of the primary mechanisms believed to fuel this  $\gamma$ -ray emission is the interaction between high-energy cosmic rays (CRs) and the Sun's outer layers, as well as its complex magnetic field structure. Specifically, the collisions of high-energy CRs with the solar atmosphere produce fluxes of  $\gamma$ -rays, neutrinos, antiprotons, neutrons, and antineutrons. The intensities of these fluxes hinge on the models of CR motion in the inner solar system's magnetic fields (typically portrayed by Parker's spiral structure; Parker 1965) and the postulated magnetic configurations on the solar surface. Indeed, both modeling the solar  $\gamma$ -ray emissions and reconciling them with observations remain formidable challenges to this day.

Investigating solar  $\gamma$ -ray emission presents unique challenges due to the Sun's transit against a background populated with point and extended sources, including the diffuse  $\gamma$ -ray emission associated with our Galaxy's disk. This transit

introduces a nonisotropic and time-variability component to the solar background, adding complexity to the analysis. Despite these analytical hurdles, Orlando & Strong (2008) first successfully detected the solar  $\gamma$ -ray signature using EGRET observations, revealing the components tied to the solar disk and solar halo. Upper limits with EGRET to the solar disk emission were previously obtained by Thompson et al. (1997). Subsequently, with the launch of the Fermi Large Area Telescope (LAT) mission (Atwood et al. 2009), Orlando (2009) and Abdo et al. (2011) were able to probe the solar  $\gamma$ -ray emission with improved resolution and sensitivity, providing a better identification of the disk and halo spectral components.

Building on these foundational studies, Linden et al. (2018) made significant advancements in our understanding. Their analysis used helioprojective coordinates to investigate the localization of  $\gamma$ -ray events from the solar disk, providing an unprecedented view of the emission morphology. Their work include the identification of different morphological components of the  $\gamma$ -ray emission (with variation over the solar cycle, and different spectral features) and the detection of solar disk  $\gamma$ -ray flux at energies above 100 GeV during the solar minimum (of cycle 24). They employed a Kolmogorov–Smirnov (KS) test to compare event distributions against a model of constant surface brightness, and for the first time unveiled deviations from the expected isotropic disk emission. Furthermore, Linden et al. (2022) delivered a  $\gamma$ -ray analysis of the solar disk over an entire 11 yr solar cycle and presented a detailed spectrum between 100 MeV and 100 GeV. Their work unveiled a strong

anticorrelation between solar activity and  $\gamma$ -ray emission, highlighting the role of solar atmospheric magnetic fields over cosmic-ray modulation, which influences both the  $\gamma$ -ray flux and morphology.

The disk and halo components of solar  $\gamma$ -ray emission manifest distinct spatial and spectral characteristics. The compact disk emission corresponds to the solar disk angular size (of approximately  $0.26$  radius), while the halo emission extends to large angular distances around the Sun, generating a significant diffuse foreground in the  $\gamma$ -ray sky (Orlando & Strong 2021). The solar halo component is primarily attributed to inverse-Compton (IC) scattering of the solar radiation field by relativistic cosmic-ray electrons. This IC component was first modeled by Orlando & Strong (2007, 2008) and predicted to yield a flux ( $F_{\geq 100 \text{ MeV}}$ ) of  $2.18 \times 10^{-7} \text{ cm}^{-2} \text{ s}^{-1}$  within  $10^\circ$  of the Sun's center. Both EGRET and Fermi-LAT observations have confirmed this solar halo flux, aligning with the predicted estimates (Abdo et al. 2011). Other mechanisms, such as particle acceleration in solar flares and coronal mass ejections (Chupp et al. 1973; Kanbach et al. 1993; Abdo et al. 2011; Share et al. 2018; Ajello et al. 2021), are also known to induce intense  $\gamma$ -ray emissions, which can last from several minutes to hours, but with steep spectra.

The emission from the solar disk is anticipated to be mainly driven by hadronic interactions of CRs with the solar surface. Seckel et al. (1991) argued that these CRs are predominantly protons and discussed the influence of the solar magnetic field over them. Cosmic-ray protons with energy exceeding a certain threshold ( $E_t$ ) would not be affected by the solar magnetic field lines, instead penetrating the solar surface directly. These particles would generate hadronic cascades in the Sun's interior, and  $\gamma$ -rays would not be able to escape. Only CR particles with energy below  $E_t$  would interact with the magnetic field configuration and be reflected by it. The cascades from these reflected CRs would eventually include  $\gamma$ -rays that escape the photosphere and heliosphere, and these are detectable as disk emission. Seckel et al. (1991) mention that the energy threshold  $E_t$  varies depending on the solar magnetic field structure, strength, and scale under consideration, with values ranging from 300 GeV (for the “canopy, where flux tubes broaden out and merge”) to 20 TeV (for the large-scale bipolar magnetic field).

The Fermi satellite has offered a unique glimpse into the  $\gamma$ -ray sky, enabling us to observe the behavior of the Sun's MeV–GeV emissions. While our understanding of solar  $\gamma$ -ray emission is still developing, current observations provide valuable data for models incorporating spatially and temporally resolved  $\gamma$ -ray fluxes.

The recent detection of solar disk emissions at the TeV range by the High-Altitude Water Cherenkov (HAWC; Albert et al. 2023) expanded our observational knowledge and showed that solar TeV emissions anticorrelates with solar activity (i.e., a larger flux during solar minimum and a lower flux during solar maximum). In a previous work, Ng et al. (2016) used 6 yr of Fermi-LAT observations and were the first to report on the anticorrelation between solar activity and the GeV solar disk emission. The same modulation in the GeV band was later confirmed by Linden et al. (2022) over an entire solar cycle (11 yr), in line with HAWC's measurements in the TeV band. Albert et al.'s (2023) observations with HAWC explores the energy range from approximately 500 GeV to 2.6 TeV, using a data set collected from 2014 November to 2022 January. These

observations suggest the corresponding spectral index to be  $3.62 \pm 0.14$ , which is steeper than the CR spectrum. Given that the spectrum observed by Fermi-LAT in the GeV band is harder than the CR spectrum, HAWC data suggest a spectral break at approximately 400 GeV. This sets a crucial constraint for models aiming to reproduce solar emissions at very high energies.

Mazziotta et al. (2020) employed the FLUKA code (a Monte Carlo code for simulating hadronic and electromagnetic interactions; Ferrari et al. 2005; Böhlen et al. 2014) to simulate CR interactions with the Sun, incorporating a detailed account of the physical environment. The model used by Mazziotta et al. (2020) considers (i) protons, helium, and electrons as primary CR components, with energy levels ranging from 100 MeV to 100 TeV; (ii) the development of CR cascades along the solar atmosphere, modeled using a density profile; (iii) the flux of CRs reaching the Sun, estimated based on the CR flux observed from Earth (as measured by AMS-02), and accounting for the propagation of CRs through the solar system up to the Sun (i.e., setting the flux at 1 au based on the CR flux at Earth); and (iv) a detailed magnetic field representation, using the potential field source surface (PFSS) model (Altschuler & Newkirk 1969; Schatten et al. 1969) and the Bifrost stellar atmosphere simulation code (Gudiksen et al. 2011; with enhanced descriptions of solar flux tubes and the chromosphere). According to Mazziotta et al. (2020), protons, helium, and electrons contribute 74%, 24%, and 2% to the solar  $\gamma$ -ray emission, respectively.

Several other notable works have estimated solar disk  $\gamma$ -ray emissions, including Li et al. (2020), and Zhou et al. (2017), which used the Geant4 toolkit (Agostinelli et al. 2003) for simulating particle propagation through matter. These simulations revealed that the primary channel for solar  $\gamma$ -ray production is the decay of neutral pions generated via proton–proton interactions (involving cosmic-ray protons and thermal protons in the solar plasma) or subsequent hadronic showers. A contribution of around 10% comes from electron and positron bremsstrahlung and positron annihilation, primarily during the final stages of secondary cascade showers. In addition, recent theoretical advancements by Li et al. (2024) provide a model for small-scale magnetic fields and describe its contributions to shape the  $\gamma$ -ray spectral emission from the solar disk. In all cases mentioned, the observed flux for energies greater than 10 GeV deviates from the simulations and models, exhibiting a harder spectrum than expected.

In a study with Fermi-LAT data, Tang et al. (2018) reported a high-energy spectral signature in the solar  $\gamma$ -ray spectrum, resembling a spectral dip or flux gap in the 30–50 GeV band. The origin of this spectral feature remains unclear and deepens the mystery surrounding the solar disk  $\gamma$ -ray surplus (which can exceed the expected flux by nearly an order of magnitude at the highest energies). Furthermore, recent simulations (Li et al. 2020; Mazziotta et al. 2020) provide no insight into the reported spectral dip signatures at about 30–50 GeV.

A recent proposal by Banik et al. (2023) posits that the Sun, during its quiet states, could function as a Tevatron, accelerating CRs up to TeV energies. In this model, protons confined within the chromosphere's magnetic field gain energy through shock acceleration (“acoustic-shock disturbances moving upward in the solar atmosphere”). Given the chromosphere's size, it can contain magnetically trapped TeV protons that interact with matter in the solar atmosphere, resulting in

detectable  $\gamma$ -ray and neutrino signals. This approach can replicate the observed  $\gamma$ -ray spectrum continuum (including Fermi-LAT and HAWC data) and deserves further investigation. Yet, the puzzling spectral dip remains unexplained.

In a previous work, Linden et al. (2018) report on the solar disk  $\gamma$ -ray emission becoming “more polar after the solar minimum” (of cycle 24) and that this trend increases significantly at higher energies. In that case, Linden et al. (2018) studied solar disk samples with events before and after 2010 January (respectively covering 17 and 94 months each) and later in Linden et al. (2022) incremented the study with data up to 2020. We now have the opportunity to extend their analysis, considering extra 3 yr of Fermi-LAT data and looking into different subsamples regarding solar activity, energy, and time. We look forward to drawing a better understanding of the trends observed in past studies and to develop new data exploration and visualization strategies.

Here in this work, we focus on the solar disk emission component, which dominates at GeV energies. We localize  $\gamma$ -ray events within helioprojective coordinates (Fränz & Harper 2002), tracking their occurrence in relation to the Sun’s center and rotation axis. We further explore dependencies in connection with the energy band, solar cycles, and polar magnetic field strength. In selecting our  $\gamma$ -ray sample, we use a 5 GeV energy cut in order to restrict the analysis to events with high angular resolution. At this energy level, we also circumvent potential contamination from solar flares (Ajello et al. 2021). Linden et al. (2022; their Figure 2) show the Fermi-LAT spectrum from 2008 to 2020, comparing between the entire data set and a case where solar flares were removed, which mostly affects the  $\gamma$ -ray flux at  $E < 1$  GeV.

In addition, we take careful measures to account for the presence of foreground contaminants, including the Earth’s limb, Sun–Moon encounters, and the presence of background high-energy/astroparticle sources, primarily: The third data release from the fourth Fermi Large Area Telescope catalog of gamma-ray sources (4FGL-DR3; Ajello et al. 2020; Abdollahi et al. 2022), the second catalog of flaring gamma-ray sources from the Fermi-LAT All-sky Variability analysis (2FAV; Abdollahi et al. 2017), and blazars and blazar candidates from multiple catalogs (Masetti et al. 2013; Arsioli et al. 2015; Massaro et al. 2015; Arsioli & Chang 2017; Chang et al. 2017, 2019; Arsioli et al. 2020). In addition, we considered the first catalog of Fermi-LAT Long Term Transient sources (1FLT; Baldini et al. 2021) but found no match (in space and time) between the solar transits and the 1FLT transient events.

With this work, we study the  $\gamma$ -ray emission from the solar disk using model-independent statistical tests. We investigate the existence of anisotropic signatures in  $\gamma$ -ray emission and explore dependencies regarding energy and time.

## 2. The Solar Disk Refined Sample

This study investigates the distribution of  $\gamma$ -ray events associated with the solar disk. The data come from observations made by the Fermi-LAT satellite from 2008 August to 2022 January.<sup>6</sup> Our event selection is carefully designed to account for any background events that could potentially taint the final sample. Such background events include Sun–Moon

encounters, the Sun’s transit across the galactic disk, proximity to 4FGL  $\gamma$ -ray perennial and transient sources, proximity to blazars and blazar candidates, and coincidences with  $\gamma$ -ray bursts (GRBs) listed in the Fermi-LAT  $\gamma$ -ray burst monitor (GBM) catalog.

The Fermi-LAT event files (FT1) provide essential information about each event such as energy, sky position (R.A. and decl. in J2000), time of occurrence, zenith angle, event-ID, event class, and event type. For the event class, the classification is based on the photon probability and the quality of the event reconstruction. Each event class is characterized by its own set of instrument response functions. For the present analysis we have selected a sample of P8R3-SOURCE events (evclass = 128), which are recommended for the analysis of moderately extended sources and point sources on medium to long timescales. The average point-spread function (PSF) for these events is approximately  $0^\circ.16$  at 10 GeV and asymptotically approaches  $0^\circ.10$  above 50 GeV.

Events within each class are further divided into different event types, according to selections based on event topology. In particular, in the Fermi-LAT PASS8 release (Atwood et al. 2013), each event is assigned a PSF event type, indicating the quality of the reconstructed direction. Events are divided into quartiles, designated as PSF0 (lowest-quality quartile, evtype = 4), PSF1 (evtype = 8), PSF2 (evtype = 16), and PSF3 (highest-quality quartile, evtype = 32). While we follow up on PSF0 events, it is important to note that we do not use them in our analysis due to their relatively large PSF. The PSF 68% containment radius varies with energy and event type. For instance, at 10 GeV, this value is approximately  $0^\circ.17$  for PSF1,  $0^\circ.12$  for PSF2, and  $0^\circ.08$  for PSF3, as described in the Fermi-LAT PASS8 documentation.<sup>7</sup>

To follow up on the individual event’s PSF, we use *gtselect* to prepare a preselection and build four separate all-sky subsamples, respectively with PSF0 to PSF3.<sup>8</sup> At this preselection stage, we recover all-sky events with energy exceeding 2.5 GeV and with a maximum zenith angle of  $110^\circ$ . For each subsample, we use *gtmktime* to filter only good time intervals, with data quality assigned by the flags (*DATA\_QUAL* > 0)&&(LAT\_CONFIG==1). Throughout our sample selection, we will examine the use of different source-type events, focusing on events with the most accurately reconstructed positions.

To accurately locate the Fermi-LAT observatory at the time of each event, and to track the positions of the Sun and Moon relative to it, we rely on additional information available in the spacecraft files (FT2).<sup>9</sup> The Fermi-LAT FT2 files provide the Sun’s position (RASUN, DECSUN [J2000]); however, the Moon’s position needs separate computation and subsequent incorporation into the FT2 database. To accomplish this, we employed the Moonpos-1.2 tool,<sup>10</sup> which factors in parallax correction to account for Fermi-LAT’s continuous positional shift.

<sup>7</sup> Fermi-LAT PASS8 PSF: [https://www.slac.stanford.edu/exp/glast/groups/canda/lat\\_Performance.htm](https://www.slac.stanford.edu/exp/glast/groups/canda/lat_Performance.htm).

<sup>8</sup> We use *gtselect* with *evclass* = 128 and *evtype* corresponding to PSF0, PSF1, PSF2, and PSF3 to create four subsamples that separate events according to their PSF types.

<sup>9</sup> Cicerone: [https://fermi.gsfc.nasa.gov/ssc/data/analysis/documentation/Cicerone/Cicerone\\_Data/LAT\\_DP.html](https://fermi.gsfc.nasa.gov/ssc/data/analysis/documentation/Cicerone/Cicerone_Data/LAT_DP.html).

<sup>10</sup> Moonpos-1.2, a user contribution tool, was authored by Dr. Paul Ray and has recently been updated: <https://fermi.gsfc.nasa.gov/ssc/data/analysis/user/>.

<sup>6</sup> For a comprehensive description of the Fermi-LAT mission, including a detailed discussion on instrument performance, calibration, and the associated ScienceTools, readers are invited to consult Atwood et al. (2009) and Fermi Science Support Development Team (2019).

**Table 1**  
In This Table We List the GRBs that Happen Close to the Sun

GRB ID	MJD	Date	R.A. <sub>grb</sub>	Decl. <sub>grb</sub>	R.A. <sub>☉</sub>	Decl. <sub>☉</sub>	$T$ start (MET)	$T$ en (MET)
GRB100207721	55827.48	2010Feb07	321.78	−15.78	321.112	−15.225	287254160.6	287291960.6
GRB110923481	55827.48	2011Sep23	181.37	−1.60	179.941	0.0256	338468450.6	338506250.6
GRB121005030	56205.03	2012Oct05	195.17	−2.09	191.044	−4.7472	371088849.6	371126649.6
GRB150705009	57208.00	2015Jul05	102.49	20.86	103.565	22.8517	457746018.6	457783818.6
GRB200922718	59114.72	2020Sep22	182.02	−1.96	179.883	0.0511	622485846.6	622523646.6

**Note.** In the following columns, we specify the GRB name according to the Fermi GBM Burst Catalog (GRB<sub>yymmddff</sub>, i.e., year (y), month (m), day (d), fraction day (ff)), the MJD time associated to the GRB event, the date, the R.A. and decl. positions associated with the GRB, the solar position at the time (R.A.<sub>☉</sub>, decl.<sub>☉</sub>), and the time windows removed (from  $T$  start to  $T$  end) in units of Mission Elapsed Time (MET).

The FT2 files contain the spacecraft’s position at 30 s intervals. We cross-matched the event files (FT1) with the spacecraft files (FT2), thereby assigning the spacecraft, Sun, and Moon positions at the time of each event. We employed a 30 s time bin and retained the closest match between FT1 event time and FT2 spacecraft time. With this data, we calculated the distance between the Sun and each  $\gamma$ -ray event within our sample. Additionally, we determined the distance between the Sun and the Moon at every time, so that we can account for Sun–Moon transits.

### 2.1. The Base Sample

We start our analysis with a selection of events within  $0.5^\circ$  of the solar center, with energies exceeding 5 GeV, zenith angles larger than  $105^\circ$ , and PSF1-2-3.<sup>11</sup> This effectively eliminates PSF0 events associated with the poorest directional reconstruction and spatial uncertainty, enabling us to concentrate on solar disk emission. This preliminary selection yields 1125 events, which hereafter will be designated “base sample.”

The base sample selection emphasizes our focus on solar disk emission, which predominates over the IC component at GeV energy levels. Given the solar disk’s angular radius of  $r_\odot \approx 0.26^\circ$ , the base sample encompasses an area approximately twice the size of the solar disk. The zenith-angle cut, following recommendations from Ajello et al. (2017), serves to exclude  $\gamma$ -ray events that might arise from CR interactions with the Earth’s atmosphere.

### 2.2. The Clean Sample: Foreground Cleanup

In this section, we detail additional cuts to the base sample intended to minimize association of spurious events with the solar disk. We describe a sample selection that accounts for solar transits through the galactic disk, Sun–GRB coincidences, Sun–Moon encounters, and the solar transit through known (and candidate)  $\gamma$ -ray sources. As for the resulting selection, we refer to it as the “clean sample.”

**Galactic Cut.** The galactic disk is a significant source of nonisotropic  $\gamma$ -ray foregrounds. To reduce this effect, we exclude 180 events from the base sample that occur while the Sun transits through the galactic disk (at lower galactic latitude  $|b| < 10^\circ$ ).

**GRBs.** Using the Fermi GBM Burst Catalog<sup>12</sup> (von Kienlin et al. 2020), we noted the dates and positions of listed GRBs,

identifying any within  $5^\circ 0$  of the Sun. We then removed a time window of 30 minutes before and 10 hr after each GRB occurrence, as outlined in Table 1. Despite the solar-GRB encounters listed, this cut did not result in the removal of any events from the current sample (i.e., the base sample just after the galactic cut).

**Sun–Moon Transits.** The MoonposV1.2 tool provides reliable calculation of the Moon’s positions (including parallax corrections) and was used to determine the Sun–Moon encounters. The Moon is known to emit  $\gamma$ -rays, a consequence of pion decay from CRs bombarding the lunar surface (Moskalenko & Porter 2007; Ackermann et al. 2016). The lunar  $\gamma$ -ray spectrum at the GeV band is relatively steep (Johannesson & Orlando 2013; Ackermann et al. 2016) and faint in comparison to the solar disk GeV emission. Though it is unlikely to constitute a significant contaminant for the GeV component of solar disk emission, we removed all time windows related to Sun–Moon encounters within a distance of less than  $2^\circ 0$ . This resulted in the removal of one event compared to the previous step.

**The Background of  $\gamma$ -Ray Sources.** A source of contamination for the solar disk emission in the GeV–TeV band is the presence of  $\gamma$ -ray sources along the Sun’s path. We account for this by considering all sources in the 4FGL-DR3 catalog (Abdollahi et al. 2022) and the 2FAV list of flaring  $\gamma$ -ray sources (which encompasses transients that could potentially contaminate our sample; Abdollahi et al. 2017). Notably, sources known to exhibit extended  $\gamma$ -ray emission are flagged accordingly. We further include all blazars and robust blazar candidates from a series of catalogs (Masetti et al. 2013; Arsioli et al. 2015; Massaro et al. 2015; Arsioli & Chang 2017; Chang et al. 2017, 2019; Arsioli et al. 2020). Even if undetected in broad-time, broadband Fermi-LAT analysis, blazars and blazar candidates are potential  $\gamma$ -ray transients (detectable only in short time windows; Arsioli & Polenta 2018). This process results in a compilation of approximately 13.5 k entries, around 11 k of which are located at high galactic latitude  $|b| > 10^\circ$  and may contaminate our sample in case of a solar transit.

On an event-by-event basis, we used the Astropy<sup>13</sup> Python library (Astropy Collaboration et al. 2013, 2018, 2022) to compute the distance between the solar center and the nearest contaminant sources. We excluded all intervals where the Sun-to-source distance is  $\leq 0.6^\circ$ . For extended sources, we implemented a larger Sun-to-source distance threshold of  $1^\circ 0$ . This procedure resulted in the removal of 211 events.

<sup>11</sup> Here, we select events from the preselection, as described in Section 2.

<sup>12</sup> The continuously updated GBM Burst Catalog, also referred to as “The FERMIGBRST database,” is available at <https://heasarc.gsfc.nasa.gov/W3Browse/fermi/fermigbrst.html>.

<sup>13</sup> Astropy: <http://www.astropy.org>.

**Table 2**

The First Column Presents the Subsample Short Name, Following the Data Selection Described in Section 2

Subsample	Number of Events with:			
	$E \geq 5$	$E \geq 8$	$E \geq 20$	$E \geq 50$ GeV
Base sample	1125	628	180	52
Gal-cut	945	539	148	38
Sun-GRBs	945	539	148	38
Sun-Moon	944	538	147	38
Sun-sources	730	422	109	28
Refined sample	419	317	109	28

**Note.** The subsequent columns shows the number of events “n” with energies  $E \geq 5, 8, 20,$  and  $50$  GeV. It should be noted that the energy levels of 5, 8, and 20 GeV are aligned with those used to construct the refined sample. An additional 50 GeV level is included to monitor the number of highest-energy events.

Through this process, we ensure that even short-lived  $\gamma$ -ray transients (associated with blazars and blazar candidates) are accounted for on a case-by-case basis, and any potential contaminants are duly removed from our sample. We implemented all time and energy selection in a custom Python script, including cuts associated with the zenith angle of events, galactic latitude, Sun-Moon encounters, Sun-GRB encounters, Sun-source encounters, and event type. The resulting clean sample contains 730 events with  $E \geq 5$  GeV.

### 2.3. The Refined Sample: Quality of Event Reconstruction

The main objective of our study is to inspect the localization of  $\gamma$ -ray photons that originate from the solar disk. In doing so, it is essential not only to build a clean sample but also to ensure that it includes only well-reconstructed events. Given that the solar radius ( $r_{\odot} \approx 0^{\circ}.26$ ) represents the characteristic angular scale of our system, we require that all events exhibit a characteristic PSF scale smaller than half the solar radius, i.e.,  $0^{\circ}.13$ . This PSF-based selection ensures a precise event localization that is crucial for our examination of the solar disk’s  $\gamma$ -ray morphology, thereby bringing novel insights into its behavior.

Based on this consideration, we have implemented a further energy-dependent event selection to obtain a refined event sample. In the energy range 5–8 GeV we have retained only PSF3 events; in the energy range 8–20 GeV we have retained only PSF2 and PSF3 events; and finally, for energies above 20 GeV we have retained only PSF1, PSF2, and PSF3 events.

Table 2 presents the event count for the base sample to the refined sample. We examine the sample sizes at each selection stage, counting all events with energy exceeding 5, 8, 20, and 50 GeV. Note, the base sample includes events occurring within  $0^{\circ}.5$  of the Sun center, with  $E > 5$  GeV, zenith angle  $\leq 105^{\circ}$ , and PSF1-2-3. Subsequent selection steps aim to cleanse the sample, with the final stage focusing on refining it to include only the best reconstructed events.

When considering all events with PSF1-2-3, the primary reason for the drop in the number of events in the energy range between 5 and 20 GeV is the stringent quality of reconstruction requirements set by the refined sample, leading to a reduction of 43%–25%, respectively. Next, the galactic cut significantly impacts all energy ranges, removing between 15% and 25% of the base sample events, from the lowest to highest energies. The process of accounting for solar encounters with detected

and potential  $\gamma$ -ray sources is another crucial step in refining the sample, which results in the elimination of approximately 25% of events across all energy ranges. The cuts related to GRBs and Moon transits have the least impact on the final sample size.

The data presented in Table 2 are noteworthy for four key reasons: (i) the potential contamination from solar encounters with  $\gamma$ -ray sources and transients is significant, and accounting for those encounters lead to the removal of approximately 25% of the events; (ii) at energy levels  $\geq 5$  GeV and outside the galactic disk, the contamination of solar disk emission due to GRBs and Moon transits is relatively low; and (iii) the solar disk remains a significant emitter at  $E > 20$  GeV, even after all data cuts, and this holds true for the best event types 16 and 32.

### 2.4. The VHE Events at $E > 90$ GeV

In Table 3 we list all events with  $E \geq 90$  GeV from a cone with  $0^{\circ}.5$  angular aperture centered on the Sun and with a zenith angle of up to  $110^{\circ}$ . We take into account all events types (i.e., PSF0 to PSF3) and monitor the point in our selection at which each event is eliminated.

We identified a total of 16 events with  $E > 90$  GeV, and more than a third survived the selection steps that led to the clean sample. Removed events (and its corresponding numbers) include: three PSF0 events, another four occurred during solar transits through the galactic disk (at  $|b| \leq 10^{\circ}$ ), two were removed due to close proximity with potential  $\gamma$ -ray emitters, and one had a zenith angle of  $\approx 106^{\circ}$ . The events removed due to close proximity with sources involved a confirmed blazar 5BZQ J0848+1835 and the blazar candidate CRATES J041840+211632. Despite implementing stringent sample refinement criteria, six events with  $E > 90$  GeV survived, with the highest-energy event of 138.4 GeV. Our analysis confirms the solar disk as a very-high-energy (VHE) emitter, extending the findings from Linden et al. (2022) and in line with recent measurements from HAWC (Albert et al.; 2023).

## 3. Localization of Solar Disk $\gamma$ -Rays: Helioprojection

Our refined sample now holds the best reconstructed events (all with characteristic PSF smaller than  $\approx 0^{\circ}.13$  and  $E > 5$  GeV) out of the galactic disk  $|b| > 10^{\circ}$  and that survived the sample selection regarding solar close encounter with the Moon, GBRs and  $\gamma$ -ray sources/transients/candidates. We use the Python library SunPy<sup>14</sup> (Mumford et al. 2020) to convert the events positions into a helioprojection (Fränz & Harper 2002). SunPy includes parallax correction due to the observer’s motion with respect to the observed target (which causes apparent displacement of the target when viewed from different positions).

The helioprojection converts the positions of events observed with Fermi-LAT (R.A., decl. in J2000) into a reference frame with origin at the solar disk center and with axis directed along the Sun’s rotation axes ( $T_y$ ) and perpendicular to it ( $T_x$ ). In Section 4, we describe model-independent statistical tests considering subsamples with the entire data set (from 2008 August to 2022 January) but also for subsamples corresponding to time intervals centered on the maximum (max) and minimum (min) solar activity. Based on considerations regarding the CR spectrum and the solar activity (sunspot

<sup>14</sup> SunPy: <https://sunpy.org/>.

**Table 3**  
This Table Provides a List of All Events with  $E > 90$  GeV that Occur within  $0.5^\circ$  of the Sun and Have a Zenith Angle up to  $110^\circ$

$E$ (GeV)	PSF	R.A.	Decl.	B	Zenith	Dist-Sun (deg)	Event ID	Time (MET)	Removed
117.2	PSF1	1.336721	0.703271	-60.0	40.4	0.254	6168824	2.594042e+08	...
112.6	PSF1	235.905228	-19.473272	27.4	54.2	0.287	13163357	2.803965e+08	...
95.7	PSF2	302.758575	-20.092472	-26.1	44.1	0.148	1665684	2.541428e+08	...
138.4	PSF2	144.415894	14.299705	43.2	59.2	0.260	7244859	2.719917e+08	...
92.9	PSF2	228.499466	-18.012501	33.1	28.2	0.081	6772459	2.797988e+08	...
94.5	PSF3	161.036316	8.175216	54.4	57.6	0.148	7193764	3.366444e+08	...
212.8	PSF0	224.497284	-16.850988	36.3	47.4	0.067	7567307	2.478953e+08	PSF
103.2	PSF0	260.345856	-23.102371	7.7	76.9	0.398	5095854	2.508446e+08	PSF
162.3	PSF0	326.701416	-13.468830	-44.8	70.5	0.360	7285392	5.402370e+08	PSF
467.6	PSF1	268.045502	-23.177397	1.7	52.9	0.337	3623019	2.829892e+08	gal-cut
226.8	PSF1	272.899139	-23.342749	-2.2	21.7	0.068	5799030	2.517901e+08	gal-cut
126.1	PSF1	265.657532	-23.281782	3.5	99.0	0.105	372387	5.036870e+08	gal-cut
139.3	PSF2	260.706970	-23.243065	7.3	55.5	0.126	3030273	2.508316e+08	gal-cut
320.0	PSF1	64.301765	21.224283	-20.6	36.6	0.254	7858649	6.438328e+08	bz-cand
97.6	PSF2	130.834869	18.362808	32.6	5.9	0.195	1057159	3.022988e+08	bz
150.6	PSF2	223.126266	-16.625463	37.3	106.2	0.269	12063477	5.002214e+08	zenith

**Note.** The upper section of the table enumerates events that survived our selection process, while the lower section lists the events that were removed due to their type (PSF), their location within the galactic plane (gal-cut), their proximity to a blazar (bz) or a blazar candidate (bz-cand), or their zenith angle being greater than  $105^\circ$ .

number; Upton & Hathaway 2023), we define the following periods associated with solar maxima and minima:

1. First minimum (Min1): from 2008 August to 2011 July (MET 239557417.0-331171202.0)
2. First maximum (Max1): from 2011 July to 2016 January (MET 331171202.0-473299204.0)
3. Second minimum (Min2): from 2016 January to 2022 January (MET 473299204.0-662774405.0)

For the data analysis, we merge the two periods associated with solar minimum (Min1 + Min2), which we refer to as “Min1p2” in the text and plot legends.

### 3.1. A Look into the Radial Distribution of Events

In this section, we present the radial distribution of events for the Min1p2 and Max1 samples. We study the event distribution considering all events in the refined sample, which have energies ranging from 5 GeV to 140 GeV and a characteristic PSF of approximately  $\approx 0.13$  or better.

We select a region around the solar disk, extending from the center to  $r_{\text{out}} = 0.24$ , with a total area of  $\pi r_{\text{out}}^2$ . We divide this region into  $n_i = 13$  rings of equal area  $\pi r_{\text{out}}^2 / n_i$ . We measure the density of events along the solar radius by counting the number of events that occur within each ring and divide by the ring area. The error bars for the density are calculated as the square root of the counts divided by the ring area; here we assume that the counts in each ring are Poisson distributed. In Figure 1, the bins (i.e., the ring borders) are highlighted with the marker “|” over the dotted-dashed black line.

The radial distribution of events for the Min1p2 and Max1 samples, as shown in Figure 1, provides insightful observations. Fitting the  $E > 5$  GeV events with a broken linear function, we measure the break ( $r_{\text{break}}$ ) at approximately  $0.264$  and  $0.265$  for the Min1p2 and Max1 samples, respectively. These measurements are consistent with the angular size of the solar disk ( $\approx 0.26$ ). The fact that the break corresponds closely to the solar disk’s angular size is a significant observation. It suggests that the emission in our refined sample is

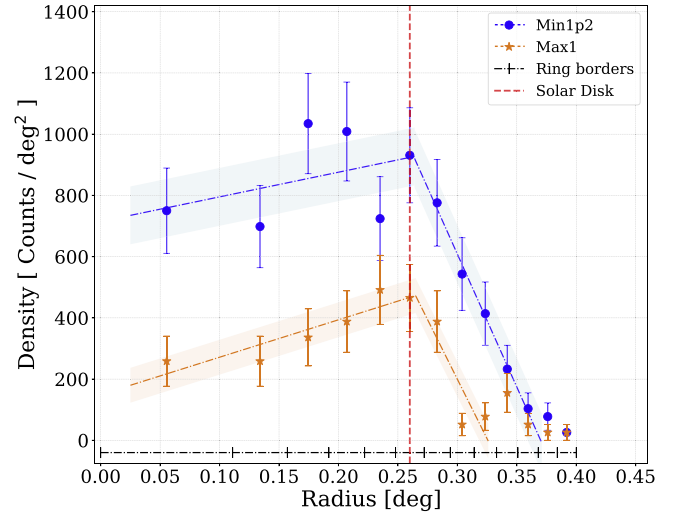


**Figure 1.** The radial distribution of events for the Min1p2 (blue) and Max1 (orange) samples, considering all events with  $E > 5$  GeV. We highlight the solar disk angular size with a red dashed vertical line. In the bottom of the plot, we show the border of the rings (bins) of constant area, over which we count events. The bins are marked with “|” over the black dotted-dashed horizontal line. The blue (orange) dotted-dashed line represents a broken linear fit (blf) to the radial density of events for the Min1p2 (Max1) sample, with its corresponding  $1\sigma$  uncertainty.

predominantly from the solar disk. If a substantial contamination were present, we would not expect the  $r_{\text{break}}$  to align with the solar disk’s angular size.

In both the Max1 and Min1p2 samples, the density of events exhibits a sharp decay just outside the solar disk, reaching a relatively low density within  $0.1$  from the disk. If the  $E > 5$  GeV emission is primarily from the solar disk, a steep decrease in event counts is anticipated beyond the solar disk, which aligns with our observations. Given that the refined sample only includes events with a characteristic PSF of  $\leq 0.13$ , this sharp decay occurs within an angular scale that is consistent with the PSF size.

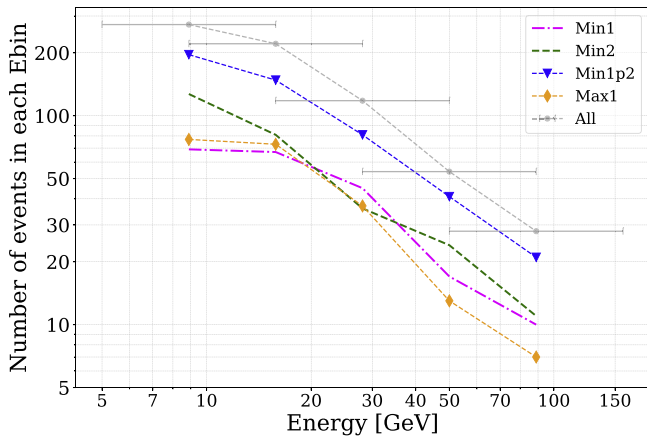


**Figure 2.** This figure represents the count of events for each energy bin. Note: this does not correspond to an intrinsic flux spectra from the Sun because the energy-dependent effects of exposure have not been taken into account. The energy bins maintain a constant size in logarithmic scale, equivalent to 0.5 dex. As a point of reference, the bin size is represented by the  $x$ -axis error bars for the data points labeled as “All.” The other labels maintain the same energy-bin size for each of their corresponding data points. The magenta dotted–dashed and the green dashed lines refer to the Min1 and Min2 subsamples, respectively. The blue triangle marker represents the Min1p2 subsample, while the orange diamond marker represents the Max1 subsample. Lastly, the gray dashed line refers to the entire sample encompassing “All” events (Max1+Min1p2).

### 3.2. A Look into the Number of Events per $E_{bin}$

To investigate the  $\gamma$ -ray emission from the solar disk, we use model-independent statistical tests to compare the distribution of events in  $T_x$  and  $T_y$  and to examine the uniformity of their circular distribution. We have performed these tests on the whole data set as well as the subsamples corresponding to the maxima and minima of the solar activity. We investigate the energy range between 5 and 150 GeV, allowing us to discern energy-dependent trends.

We define our energy bins in a logarithmic scale, each spanning a width of 0.5 dex (Allen 1951). To ensure comprehensive coverage and reduce potential biases, we overlap these bins by 0.25 dex. This means our bins cover energy ranges of approximately  $10^{0.7}$ – $10^{1.2}$  GeV,  $10^{0.95}$ – $10^{1.45}$  GeV, and so on, with a total of five energy bins. This overlapping approach enhances data visualization and minimizes biases tied to the choice of the starting energy for the bins. Figure 2 shows the number of events for each subsample and energy bin of the refined sample. It is meant to help visualize the number of events used in statistical tests that rely on the energy bins and does not incorporate exposure corrections.<sup>15</sup>

## 4. Model-independent Tests: Investigating Nonisotropic Emission

In this section, we describe our model-independent strategy for assessing signatures of anisotropic  $\gamma$ -ray emission from the solar disk. For instance, presuming isotropic emission requires a detailed model of the solar disk spectra. The spectrum dependence on energy determines the counts at a given energy bin; in turn, these counts are distributed according to the PSF and the underlying solar disk geometry. Summing these

distributions over a given energy range would lead to a biased expected distribution of events because the spectrum bears inherent uncertainties. Therefore, to investigate the solar disk emission, we focus on model-independent tests.

We analyze our data set using a combination of the KS test—a nonparametric test of the equality of continuous, one-dimensional probability distributions (Massey 1951; Darling 1957)—and the Rayleigh test, a statistical test for circular distributed data (Fisher 1953; Berens 2009). These tests offer a robust and versatile tool to examine the geometry of the  $\gamma$ -ray emissions and detect deviations from isotropy, without the constraints from predefined models.

### 4.1. KS Test

In order to investigate potential anisotropy in the  $\gamma$ -ray emission from the solar disk, we use the KS test. This test allows for a model-independent comparison of the  $T_x$  and  $T_y$  distributions of the  $\gamma$ -ray events. As there is no reason for  $T_x$  and  $T_y$  to mirror each other’s distributions (i.e., the distributions are independent), we can leverage this property to detect signs of nonisotropic emission.

The KS test compares the cumulative distribution function (CDF) of two samples, yielding a  $p$ -value that represents the likelihood that the two samples originate from the same underlying distribution. Conventionally, a  $p$ -value threshold of 0.05 is used to reject the null hypothesis, meaning the  $T_x$  and  $T_y$  distributions differ. In our exploratory analysis, we evaluate the statistical tests over five energy bins ( $n = 5$ ) within each of the independent subsamples, such as Max1 and Min1p2. To mitigate the risk of type I errors (false positives), we implement the Bonferroni correction, a well-regarded and conservative method to adjust  $p$ -values in scenarios with multiple tests (Bonferroni 1936; Hochberg 1988). We apply the Bonferroni correction separately to each independent subsample and adjust the  $p$ -value threshold to  $0.05/n = 0.01$ . We consider  $p$ -values falling below this adjusted threshold as indicative of significant anisotropic trends in the  $\gamma$ -ray emission from the solar disk.

For the KS test, we use the `KS_2samp` function from SciPy.stats Python library (Virtanen et al. 2020), specifying the two-sided test. This approach evaluates the two samples irrespective of the direction of the difference and is sensitive to any discrepancy between distributions. In the event of anisotropy in the  $T_x$  and  $T_y$  distributions, a significant disparity between the CDFs of the two samples would emerge, as determined by the KS test. It is crucial to note, however, that while the KS test can identify anisotropic trends, it does not specify their direction or nature. We feed the `KS_2samp` test with  $T_x$  and  $T_y$  values for each energy bin and for the corresponding subsamples: Min1 + Min2 (which we call Min1p2) and Max1 and separately investigate the data associated with Min1 and Min2. Figure 3 shows the  $p$ -values resulting from the KS test for the  $T_x$  and  $T_y$  comparisons.

### 4.2. The Rayleigh Test

The Rayleigh test is a powerful tool derived from circular statistics (Fisher 1953), employed to determine if a circular distribution is symmetric or exhibits deviations from uniformity. The Rayleigh test considers only the observed distribution of event angles. The test procedure involves (i) projecting the events onto a unity-radius sphere to define event-vectors; (ii) summing the vectors and normalizing the result vector by

<sup>15</sup> Therefore, Figure 2 does not represent spectral information of any kind (such as the  $\gamma$ -ray flux).

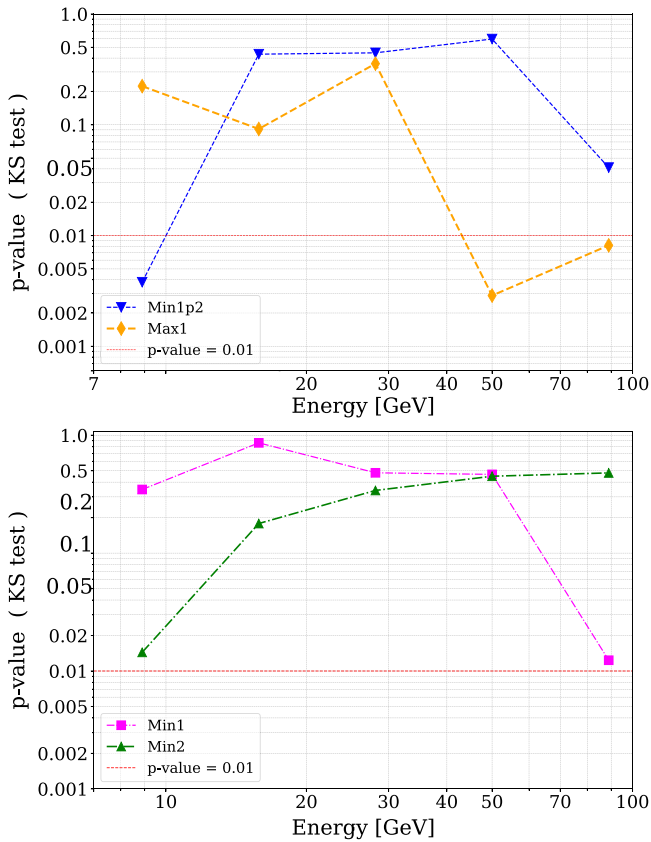


**Figure 3.** KS test  $p$ -values for each energy bin, which have a constant size in log-scale (0.5 dex), as shown in Figure 2. The red dashed line marks the  $p$ -value threshold of 0.01, below which anisotropic emission is indicated. The upper plot displays the  $T_x$  vs.  $T_y$  comparisons for the Min1p2 (blue triangle markers) and Max1 (orange diamond markers) subsamples. In the lower plot,  $T_x$  vs.  $T_y$  comparisons for the Min1 (dotted-dashed magenta line with square markers) and Min2 (dotted-dashed green line with triangle markers) subsamples are shown.

the number of event vectors used. In the ideal case of a uniform distribution, the resulting vector would be close to null. Therefore, the  $p$ -value indicates how likely the resulting vector deviates from the ideal case. This test is particularly powerful in detecting unidirectional modality (Fisher 1996; Berens 2009) and essentially measures the concentration of angles around a mean direction. In contrast, dipole or quadrupole structures in the data distribution would be harder for the Rayleigh test to resolve. As Brazier (1994) demonstrates, the Rayleigh test is sensitive to small deviations from uniformity in circular data, even for relatively small samples. To implement the Rayleigh test, we first calculate the events’ positions in polar coordinates, assigning a radius and angle to each solar disk event. We then use the *astropy.rayleightest* library<sup>16</sup> to evaluate the distribution of event angles, and Figure 4 shows the  $p$ -values resulting from the Rayleigh test.

#### 4.3. Visualization of the Events’ Localization, Density, and Distributions

The KS and Rayleigh tests showed the presence of significant anisotropic trends, with  $p$ -values going below 0.01 for the energy bins at 9 GeV (Min1p2) and 50–90 GeV (Max1).

<sup>16</sup> *astropy.rayleightest*: <https://docs.astropy.org/en/stable/api/astropy.stats.rayleightest.html>.

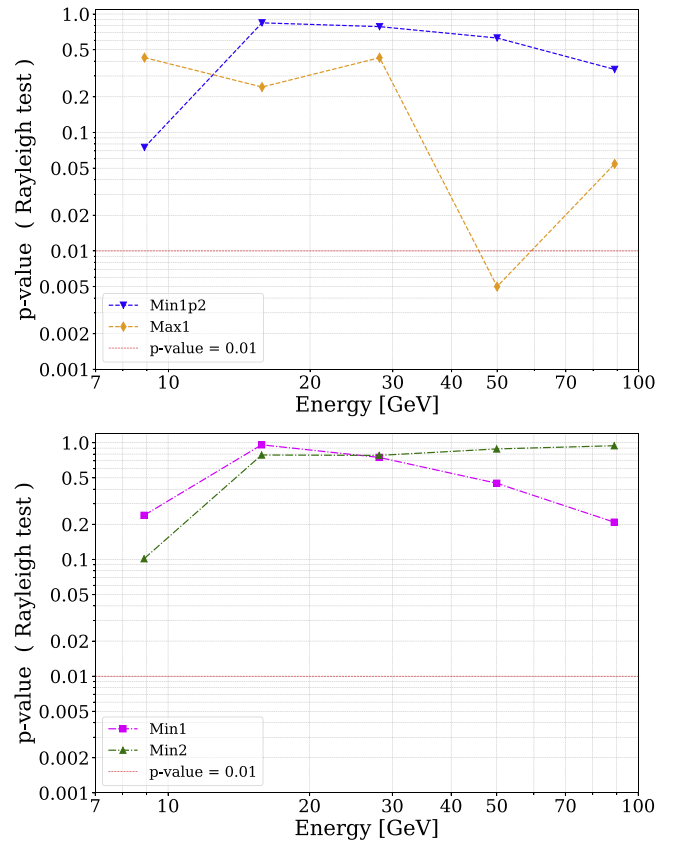


**Figure 4.** Rayleigh  $p$ -values corresponding to each energy bin. The energy bins have a constant size in log-scale (corresponding to 0.5 dex), just as in Figure 2. A red dashed line highlights the  $p$ -value threshold of 0.01, below which nonuniformity is indicated. In the upper plot, the blue triangle marker refers to the Min1p2 subsample, while the orange diamond marker indicates the Max1 subsample. In the lower plot, dotted-dashed lines in magenta and green (with square and triangle markers, respectively) refer to the Min1 and Min2 subsamples.

To better investigate and visualize those statistical results, we implement a series of diagnostic plots (Figure 5), which we describe in this section.

*The Localization of Events.* In the first row of Figure 5 we depict the localization of individual events across the solar disk. In each plot we employ color-coding to represent the energy levels (as defined in the color bar). For easy differentiation between the lowest to highest-energy events, the marker size reflects the magnitude of the event’s energy along all plots (i.e., with “small to large markers” covering the energy range between 5 and 130 GeV).

*The 2D KDE.* To better explore and visualize the results from KS and Rayleigh tests, we implement a kernel density estimate (KDE) of the event distribution. Instead of using standard KDE functions, we employ a custom 2D KDE approach that allows for varying bandwidths based on each event’s PSF. Our KDE approach computes the density representation by assigning a Gaussian function to each event, centered at its position. The width  $\sigma$  of the Gaussian function is determined by the PSF associated with each event, allowing for a representation of the event’s density that accounts for the event’s reconstruction uncertainties (e.g., the 2D KDE, Figure 5). We use the *multivariate\_normal.pdf* probability density function from SciPy.stats Python library (Virtanen et al. 2020) to perform the



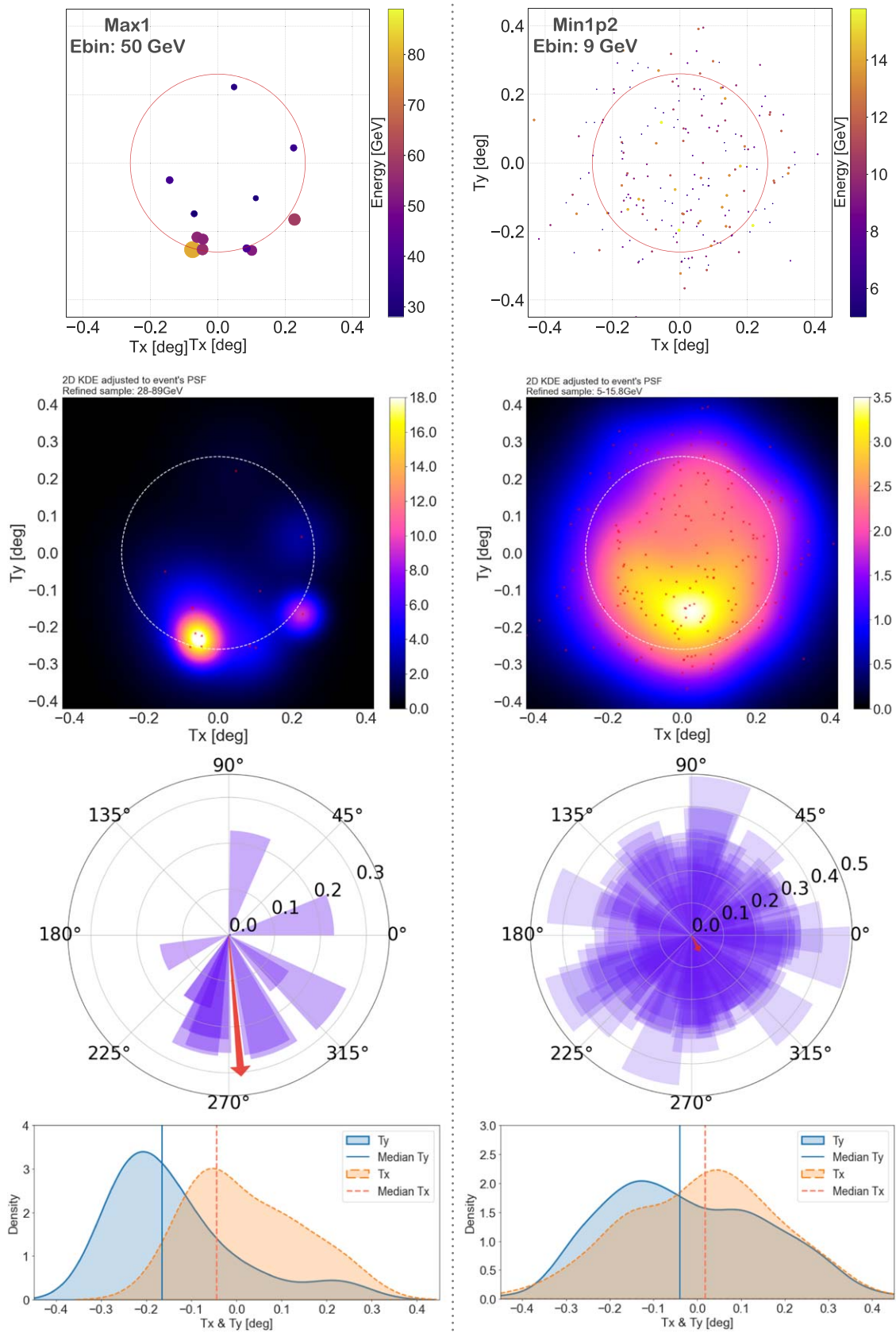


**Figure 5.** This figure presents two sets of images with visualization diagnostics for the anisotropic trends seen for the Max1 sample at 50–90 GeV energy bins (left); and for the Min1p2 sample at the 9 GeV energy bin. From top to bottom, the figure shows (i) the localization of events over the solar disk, (ii) the 2D KDE density distribution, (iii) the circular distribution of events, and (iv) the  $T_x$  and  $T_y$  histograms. All visualizations are described in Section 4.3.

2D KDE according to the equation:

$$\text{KDE}_{(x,y)} = \frac{1}{N} \sum_{i=1}^N \frac{1}{2\pi\sigma_{x,i}\sigma_{y,i}} \exp\left(-\frac{(x-x_i)^2}{2\sigma_{x,i}^2} - \frac{(y-y_i)^2}{2\sigma_{y,i}^2}\right), \quad (1)$$

where  $N$  is the number of events,  $(x_i, y_i)$  are the  $(Tx, Ty)$  coordinates of each event, and  $\sigma_{x,i}$  and  $\sigma_{y,i}$  are the PSF scales of the  $i$ th event along  $x$ - and  $y$ -axis. We assume a symmetric PSF; therefore  $\sigma_{x,i} = \sigma_{y,i}$ .

In this representation, events with smaller PSF values—indicating better localization—contribute more heavily to the density at their respective positions. In contrast, events with larger PSF values have their contributions more diffusely spread, effectively diluting their impact on the overall density. For reference, the position of individual events is marked as small red crosses. The sum of all Gaussian functions is normalized such that its integral over the entire volume equals unity. This facilitates the comparison of event concentrations across different time windows and regions, as higher values on the color bar indicate more concentrated distributions of events.

*The Circular Distribution of Events.* In Figure 5, third row, we display the circular distribution of the events over the solar disk, where each purple bar represents a single event and the bar length represents its radial position. This plot also shows the “trigonometric moment arrow” (depicted in red), which points toward a preferential direction of the event’s distribution. This arrow is calculated as the sum of unit vectors, under the assumption that the events are distributed over a circle with unitary radius. For the purposes of Figure 5 (and the following), we normalize the resulting vector assuming a sphere with a radius of  $R = 0.5$ , which better suits the angular scale of our case and offers a more reliable visualization. The arrow’s direction represents the mean angle of the circular distribution, and its length indicates the degree of departure from a circular uniform distribution. For the circular statistics, we employed the *astropy.stats.circstats* package.<sup>17</sup>

*Tx and Ty Histograms.* At the bottom of Figure 5 we show the distribution of events in  $Tx$  and  $Ty$  coordinate space, respectively shaded in orange and blue. This representation illustrates the concentration of events regarding the Sun’s rotation axis ( $Ty$ ), and perpendicular to it ( $Tx$ ), together with the corresponding median values for each distribution. Intuitively, anisotropies driven by  $Ty$  distribution shifts could be connected to long-lasting patterns of the solar polar field, while  $Tx$ -driven anisotropies would be more challenging to explain given the Sun’s rotation (i.e., the constant shift of true physical positions of the solar surface). We should note that the complexities involved in modeling CR flux impacting the solar surface are intensively explored but not fully resolved in current models (Li et al. 2020, 2024; Mazziotta et al. 2020), e.g., variations of the CR flux bombarding the solar atmosphere could play a relevant role. These models, while advanced, do not fully account for the observed fluxes above 10 GeV nor do they explain the 30–50 GeV spectral dip (Tang et al. 2018). Therefore, investigating  $Tx$  anisotropic hints is indeed relevant and might offer new insights into the intricate interactions of CRs and the solar atmosphere. Currently, it is challenging because with Fermi-LAT we need large time windows to

**Table 4**

A List of  $E > 50$  GeV Events Associated with the High-density Spot in the Max1 Sample, Located at  $Ty < -0.1$

Time (MJD)	Energy (GeV)	PSF	$Tx$	$Ty$
55784.128	52.2	PSF1	0.1010	−0.2555
55815.187	53.8	PSF1	−0.0441	−0.2227
56055.945	56.7	PSF3	−0.0454	−0.2525
56562.054	54.7	PSF3	−0.0615	−0.2167
56579.748	79.1	PSF1	−0.0749	−0.2531
57138.580	59.7	PSF3	0.2279	−0.1650

collect solar  $\gamma$ -ray events at  $E > 5$  GeV, potentially washing out  $Tx$ -driven anisotropy signatures.

## 5. Discussion: Results from KS and Rayleigh Tests

Here we discuss the results from the KS and Rayleigh tests, which were applied to subsamples in energy and which cover time windows corresponding to the solar cycles Max1 and Min1p2, as defined in Section 3.

### 5.1. The Anisotropic Trend at the Max1 Highest Energies

The Rayleigh test reveals a substantial deviation from circular uniformity for the Max1 subsample at the energy channel of 50 GeV, which translates to a preferential direction—unidirectional excess—in the circular distribution. Here, the  $p$ -value falls down to 0.005 level (Figure 4) suggesting a significant anisotropic trend in the  $\gamma$ -ray emission. For this same channel, the KS test presents  $p$ -value of 0.003 (Figure 3) and indicates the  $Tx$  and  $Ty$  distributions are different, reinforcing the evidence of  $\gamma$ -ray anisotropy.

For the Max1 sample, the trigonometric moment arrow (depicted in red, Figure 5) points toward a preferential direction, the solar south pole. The presence of anisotropic trends in both KS and Rayleigh tests provides a compelling signature of anisotropic  $\gamma$ -ray emission from the solar disk. Particularly, the 50 GeV Max1 channel has a robust sample of 13 well-localized events with energy between 28 and 89 GeV. In Table 4, we present the Max1 events that concentrate in the solar south pole (the 2D KDE plot, Figure 5).

The events associated with this high-density spot, despite being spatially concentrated, were recorded at intervals of at least 15 days, spanning nearly 750 days (between MJD 55815 to 56579; i.e., from 2011 September 1; to 2013 October 14). In terms of solar activity, this period coincides with an unusual polarity flip in the Sun (Janardhan et al. 2018; Upton & Hathaway 2023), with the south polarity flipping in 2013 November and the north polarity flip delayed by a prolonged period of nearly null radial polar magnetic field strength from 2012 June to 2014 November.

In previous observations of solar phenomena, Petrie et al. (2014) pointed out the asymmetric solar activity of the north and south poles during the transition between cycle 23 and 24, with the southern hemisphere being the most active during 2014 (during the decline of cycle 23). Therefore, asymmetry and anisotropy are common in solar physics. Petrie et al. (2014) also note that these anisotropic features are often overlooked in flux transport models, which may weaken and compromise predictions of the solar disk  $\gamma$ -ray emission. Our findings echo the known anisotropic solar activity and raise new questions about the mechanisms driving the solar  $\gamma$ -ray behavior.

<sup>17</sup> Astropy Circular Statistics: <https://docs.astropy.org/en/stable/stats/circ.html>.

### 5.2. The Min1p2 Anisotropy at the 9 GeV Energy Bin

For the  $T_x$  versus  $T_y$  comparison of the Min1p2 sample, the KS test showed  $p$ -values of 0.004 at the 9 GeV  $E_{bin}$ , indicating an anisotropic trend of the solar disk  $\gamma$ -ray emission. Nonetheless, the Rayleigh test does not reveal unidirectional excess for this same channel. Indeed, Figure 5 shows the circular momentum arrows for both Max1 and Min1p2 samples, with the Max1 arrow measuring  $0^\circ 308$  (0.617R), while the Min1p2 arrow length is only  $0^\circ 057$  (0.115 R).

Note that, for the 9 GeV energy bin, the KS tests for Min1 and Min2 samples show a strong anisotropic trend from the Min2 alone, with  $p$ -value reaching close to the 0.01 threshold. Only when considering the Min1 and Min2 sample together (i.e., Min1p2) does the significance of the anisotropic trend mount, suggesting the presence of anisotropic behavior, which the Rayleigh test was not able to resolve. Therefore, in this case, the data suggest significant deviation from the isotropic emission, which is not necessarily linked to a unidirectional excess.

### 5.3. The Energy-dependent Anisotropic Trends

The results from KS and Rayleigh test (Figures 3 and 4) highlight that the anisotropic trends are energy dependent. This observation emphasizes the potential insights gained by considering the events' distribution within discrete energy bins, rather than integrating over the entire energy range provided by Fermi-LAT observations. The observed behavior could hint at a coupling between the solar magnetic field strength and the energy channels through which the  $\gamma$ -ray photons (produced via CR interactions with the solar surface) have a higher probability of escaping. Other factors, such as variations in the density and composition of the solar surface, or even fluctuations in the incoming CR flux, could also contribute to the observed anisotropic  $\gamma$ -ray emission. Further studies with larger event samples will be necessary to investigate those hypotheses.

While the addition of data from yet another cycle observed with Fermi-LAT is likely to increase the number of measured events, the spatial concentration of those events may vary according to the solar cycle. It remains to be seen whether the Max2 period will produce a similar  $\gamma$ -ray emission pattern as observed during the Max1.

The KS test showed more flexibility than the Rayleigh test to unveil deviations in the event distributions. However, the Rayleigh test provides valuable directional information (i.e., is able to resolve unidirectional excesses) as indicated by its  $p$ -value and the corresponding circular momentum arrow. When combined, the KS and Rayleigh tests constitute a powerful tool set to investigate and compare the strength of directional excess across different time windows and energy bins. Future studies can leverage these tests to further elucidate the mechanisms driving episodes of anisotropic  $\gamma$ -ray emission from the solar disk.

To better investigate the connection between solar activity, its magnetic configuration, and the observed  $\gamma$ -ray signatures, an advanced GeV  $\gamma$ -ray observatory with enhanced sensitivity will likely be required. Such an observatory would allow us to investigate solar emission with larger samples of  $\gamma$ -ray events and with improved reconstruction capabilities to better constrain event localization. This would facilitate the analysis and interpretation of the solar  $\gamma$ -ray activity, helping to refine our understanding and complement observations across

different energy bands. Orlando et al. (2023) highlighted the significance of synchrotron radiation from galactic cosmic-ray electrons in the quiet Sun, suggesting that radio to X-ray observations can offer valuable insights into the interplay of CRs and solar magnetic fields. Furthermore, forthcoming X-ray and MeV–GeV observations from missions like FOXSI (Ishikawa et al. 2014), Gecco (Orlando et al. 2022), ASTROGAM (De Angelis et al. 2017), and AMEGO (McEnery 2017) will shed light on high-energy processes in the solar corona, while observations at TeV energies with HAWC (Albert et al. 2018), LHAASO (Cao et al. 2019), SWGO (Huentemeyer et al. 2019), and ongoing MeV–GeV studies with Fermi-LAT will further enhance our understanding of the solar disk emission at VHE.

## 6. Time Evolution of Solar Disk $\gamma$ -Ray Emission

In this section, we expand on our visualization efforts and looked forward to a temporal representations of the  $\gamma$ -ray data. Up to this point, our analysis has focused on subsamples aggregating  $\gamma$ -ray events over extensive periods, spanning multiple years (e.g., Max1, Min1p2). While this approach has been instrumental in identifying the existence of energy-dependent trends, it may obscure transient anisotropic patterns that emerge over shorter time periods. Such variations in  $\gamma$ -ray emissions could be diluted—or even completely masked—when data are summed over long time windows. To investigate the existence of transient patterns and gain deeper insights into the temporal dynamics of solar disk  $\gamma$ -ray emission, we now shift our focus to a time-resolved analysis. This approach will allow us to trace the evolution of anisotropic trends across the observational period from 2008 August to 2022 January.

To provide a comprehensive view of the  $\gamma$ -ray distribution over time, we condense six different diagnostics of the solar disk activity (described in the following paragraphs) and follow their evolution along 2008 August to 2022 January. To account for the presence of energy-dependent features revealed in our previous analysis (Section 4.3), we have divided our sample into two categories: one for lower-energy events (low- $E$ ) and another for higher-energy events (high- $E$ ). For our time analysis, we incorporate photon counts within a specific time window, which is then shifted by 100 days per frame,<sup>18</sup> so that the statistical tests are evaluated over time.

For the low- $E$  sample, we include events with energies ranging from 5 to 20 GeV. We compile these events over a 450 day time window and slide the window by 100 days for each subsequent frame (Figure 6). The high- $E$  sample includes events with energies between 20 and 150 GeV. Given the lower frequency of these higher-energy events and to ensure an adequate sample size, we use a longer time window of 700 days and slide it by 100 days for each frame (Figure 7). The selection of 450 day and 700 day time windows for the low- $E$  and high- $E$  samples is motivated by achieving a balance between the number of available events and the intended time resolution for our analysis.

For each frame we considered six types of analyses of both low- $E$  and high- $E$  samples: (i) a density plot, (ii) event localization on the solar disk, (iii) circular distribution of the  $\gamma$ -ray events, (iv) radial distribution of the events, (v) the polar

<sup>18</sup> We implement a 100 day sliding window for photon counts to balance between temporal resolution and the number of trials in our statistical analysis. For the low- $E$  and high- $E$  samples,  $n$  amounts to 45 and 42, respectively.

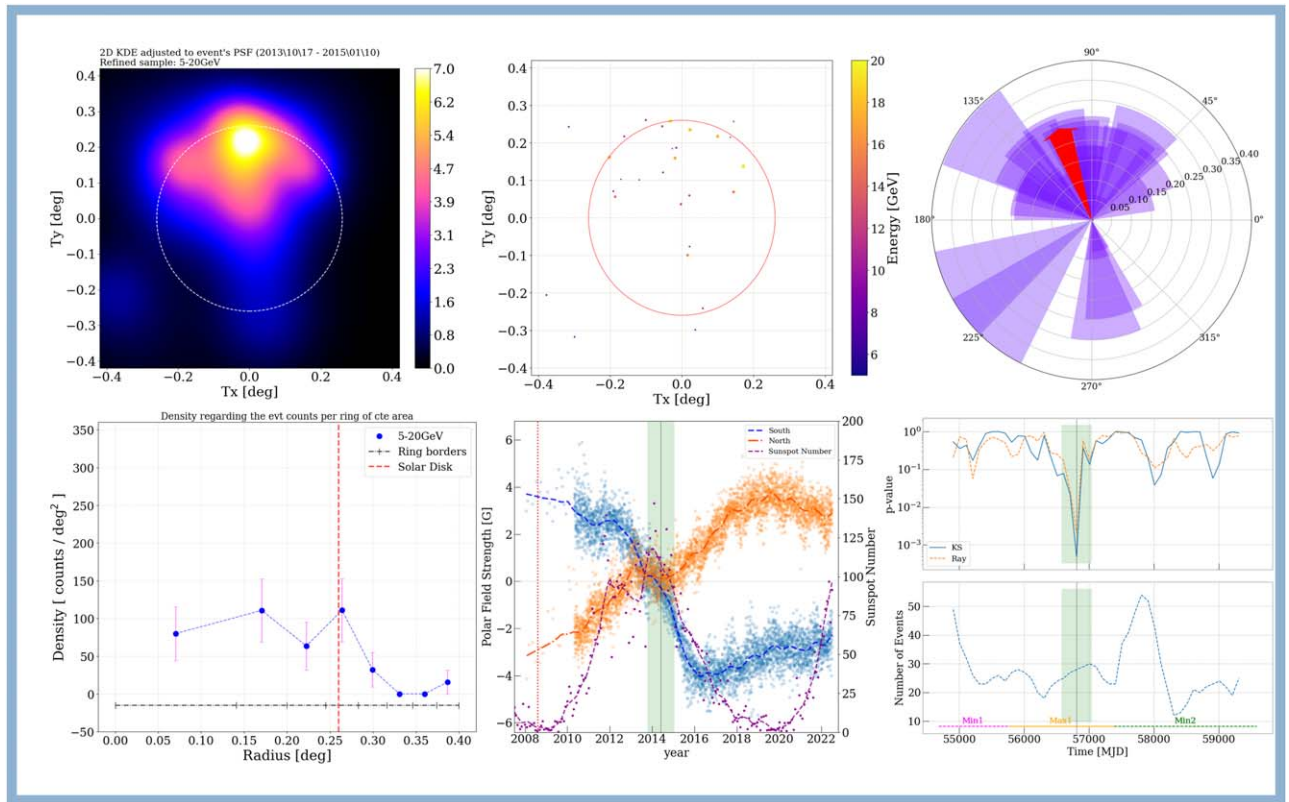


**Figure 6.** This figure presents all diagnostic plots from (i) to (vi) relating to the low- $E$  sample, which include events with energies ranging from 5 to 20 GeV. In this particular frame, the diagnostic plots are derived from a time window centered on MJD 56807.6 integrating data across a span of 450 days, from 2013 October 17 to 2015 January 10. This frame represents a period with the lowest  $p$ -values for the KS and Rayleigh tests, which coincided with the polar magnetic field flip at the maximum of cycle’s 24 solar activity.

(An animation of this figure is available.)

magnetic field strength, and (vi)  $p$ -values from the KS and Rayleigh tests, along with the respective number of events used in these statistical tests.

In the next items, we dive into the details of each plot featured in Figures 6 and 7. Essentially, those figures represent frames of an animation (provided as online material), produced when visualizing the sequence of slide frames played out.<sup>19</sup>

1. *Density Plot.* The color code represents the density of events, smoothed using a 2D KDE function that accounts for the individual event’s PSF to compute the overall density distribution (see Section 4.3). This approach is meant to highlight regions with the highest concentration of events while accounting for the event’s uncertainty in position.
2. *Localization of Events.* With each event’s position plotted over the solar disk, the color and size of each event marker represent the event’s energy, allowing a visualization of the relationship between event energy and spatial distribution. This comprehensive representation of the  $\gamma$ -ray events provides valuable insights into the correlation between energy and position, contributing to a more in-depth look into the anisotropic emission patterns.
3. *Circular Distribution.* The circular distribution highlights the  $\gamma$ -ray events’ angular positions relative to the solar disk center. The resulting vector (trigonometric momentum) measures the overall directional preference in the

distribution of events. This vector visually represents the dominant direction or trend in the event positions, aiding in the interpretation of potential anisotropy in the  $\gamma$ -ray emission from the solar disk.

4. *Radial Profile.* The radial profile depicts the distribution of  $\gamma$ -ray events as a function of their radial distance from the center of the solar disk. This profile helps identify potential irregularities in the event distribution, as discussed in Section 3.1.
5. *Polar Magnetic Field Strength.* The north and south polar magnetic field strength (left-hand y-axis) are shown. To produce this representation, we rely on the Solar Dynamics Observatory (SDO) data from its Helioseismic and Magnetic Imager (HMI) instrument, which has been providing daily coverage since 2010. We use the *drms*<sup>20</sup> Python package to access the HMI data (Glogowski et al. 2019). For the period from Fermi-LAT’s launch in 2008 August to late 2010, we supplement the data using records from the National Solar Observatory, following Janardhan et al. (2018). The dashed and dotted-dashed lines represent south and north polar fields, respectively, averaged over approximately 20 days. We also show the monthly number of sunspots<sup>21</sup> (right-hand y-axis), tracking the occurrence of the cycle 24 solar maximum.

<sup>19</sup> For visualization purpose, the animation available as online material considers frame slides by 20 days to provide a smoother, more refined view of the time evolution.

<sup>20</sup> The Data Record Management System (DRMS) developed by the Joint Science Operation Center at Stanford University.

<sup>21</sup> Sunspot counts reported at the Space Weather Prediction Center: <https://www.swpc.noaa.gov/products/solar-cycle-progression>.

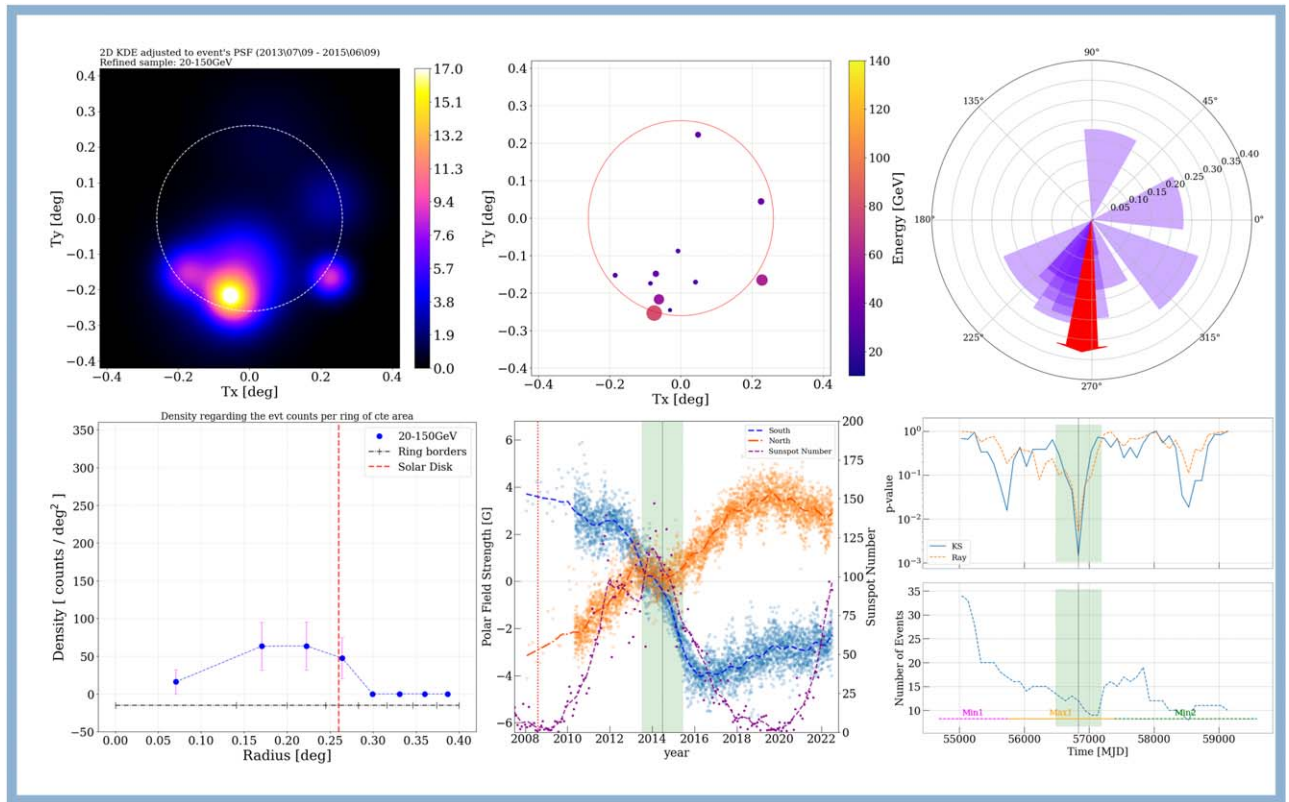


**Figure 7.** This figure presents all diagnostic plots from (i) to (vi) relating to the high-energy (high- $E$ ) sample, which include events with energies ranging from 20 to 150 GeV. In this particular frame, the diagnostic plots are derived from a time window centered on MJD 56832.6, integrating data across a span of 700 days, from 2013 July 9 to 2015 June 5. This frame represents a period with the lowest  $p$ -values for the KS and Rayleigh tests, which coincided with the polar magnetic field flip at the maximum of cycle’s 24 solar activity.

(An animation of this figure is available.)

A dashed dark-purple line represents the smoothed solar activity, which peaks around 2014 May–June. The green shaded region correspond to the time window for the current time frame.

6. *P-value Time Window.*  $P$ -values derived from KS and Rayleigh tests are shown, with the number of events regarding each sample, all plotted against time (in MJD). Note that the event counts here are not corrected for exposure; hence, they do not represent fluxes. This count is intended to demonstrate the number of events used in our statistical test and support the derived conclusions. The green shaded region represents the time window used to select the  $\gamma$ -ray events for the corresponding plots. The low- $E$  sample integrate events over a span of 450 days, while the high- $E$  sample does so over 700 days. At the bottom of this plot, the solar activity cycles are marked as Min1, Max1, and Min2.

With this approach we can resolve anisotropic episodes in time, consider energy dependencies, and explore possible connections with the solar cycles and magnetic configuration. The successful creation of these visualizations is only possible due to the well-reconstructed events in our refined sample (i.e., PSF better than  $0^\circ.13$ ) ensuring a meaningful representation of the events spatial-distribution along time. As a sound example of  $\gamma$ -ray time-analysis of the solar emission, Linden et al.

(2022) was the first to unveil the solar disk 1–10 GeV light curve over an entire solar cycle (see their Figure 5, where we contemplate the anticorrelation between the  $\gamma$ -ray flux and the solar activity) and also the first to investigate high-frequency variability of the solar disk  $\gamma$ -ray emission (i.e., looking for periodicity in flux variability) while tracking the potential origins for the signatures found in the power spectrum. In our case, by visualizing the evolution of  $\gamma$ -ray parameters associated to the solar disk (e.g., event distribution, density, radial profile of events, etc.), we look forward to valuable insights into the underlying nature of the observed emission.

In Figures 6 and 7 we highlight frames showcasing the most pronounced anisotropic trends in the low- $E$  and high- $E$  samples. From this perspective, we see that the lowest  $p$ -values occur at about MJD 56820 (2014 June) for both the KS and Rayleigh tests and both the energy samples.

With the time analysis, we now recognize an excess of 5–20 GeV events in the north pole and a corresponding excess of events between 20 and 150 GeV at the south pole. In both energy samples, the KS and Rayleigh  $p$ -values go down to  $10^{-3}$  level, indicating significant anisotropic trends in the data. The Rayleigh test suggests unidirectional excess trends in the circular distributions, with trigonometric momentum pointing to opposite directions (north and south) for the low- and high-energy samples, therefore asymmetric regarding energy. This concentration of events in the solar poles is visible from the 2D

KDE density plot, in agreement with the indications from the Rayleigh test.

Notably, this energy-dependent, dipole-like pattern coincides with a period of sign-flipping in the dipole magnetic field (refer to plot (v) in Figures 6 and 7). As pointed out by Janardhan et al. (2018), the northern polar field was nearly null from 2012 June to the end of 2014, indicative of unusual polar field behavior during this period. During the  $\approx 13.3$  yr of Fermi-LAT observations (2008 August to 2022 January), the Sun went through a single episode of polar magnetic field flip (i.e., a single solar maximum).

We can now investigate the following question: What is the likelihood that the strong anisotropic trends—observed in both the low- $E$  and high- $E$  samples—coincide with the solar maximum, only by chance?

In addressing this question, several factors need to be considered: (1) *P-value*. The  $p$ -value represents the likelihood of the  $T_x$  and  $T_y$  distributions being statistically similar (originating from the same underlying population of events). For instance, we use the values derived from the KS tests, which are the most relevant/constraining. (2) *Number of trials* ( $n$ ). To account for the number of trials, we will consider a Bonferroni correction to adjust the  $p$ -values derived from the time analysis, as detailed in Section 4.1. (3) *Coincidence with Solar Maximum*. Estimating the chance of these trends coinciding with the solar maximum (or for the polar magnetic field flip) to be approximately 1 yr, we roughly estimate a 1/13 chance of observing a significant anisotropic trend during this period, purely by chance ( $p$ -smax). (4) *Independence of Low- $E$  and High- $E$  Results*. In principle, there is no known relation between these energy ranges. Indeed, we want to evaluate if that is the case, in connection with the solar maximum (polar field sign-flip). (5) *Simultaneity of Trends*. Notably, these anisotropic trends, drawn from independent samples, occur nearly simultaneously, exhibiting energy-dependent asymmetry.

Considering these factors, the chance probability ( $p$ -low $E$ ) of observing the low- $E$  anisotropic trend during the solar maximum can be calculated as the product of the  $p$ -value, the number of trials ( $n$ ), and the chance of coincidence with the solar maximum ( $p$ -smax). This calculation results in  $0.00049 \times 45 \times 1/13 \approx 0.0017$ . Similarly, for the high- $E$  sample ( $p$ -high $E$ ), the calculation yields  $0.0015 \times 45 \times 1/13 \approx 0.0051$ .

Taking into account the independence of the low- $E$  and high- $E$  results and their simultaneous occurrence, the combined probability of observing strong anisotropic and asymmetric trends in the solar  $\gamma$ -ray emission, coinciding with the solar maximum, is estimated as ( $p$ -low $E \times p$ -high $E$ ) =  $8.7 \times 10^{-6}$ . This result, carefully accounting for the trial factor, corresponds to a statistically significant  $3.7\sigma$  signature of asymmetric  $\gamma$ -ray emission during the solar maximum.

*Time Analysis for the Entire Sample*. In Figure 8, we highlight the most pronounced anisotropic trends observed when considering the entire sample, including events with energies ranging from 5 GeV to 150 GeV (i.e., both the low- $E$  and high- $E$  samples combined). In this case, the lowest  $p$ -value occurs at about MJD 56812 (2014 June) for the KS test. Note, the Rayleigh test does not show signs of unidirectional excess, as expected in case of bipolar distribution of events; only when splitting between low- $E$  and high- $E$  events the Rayleigh is able

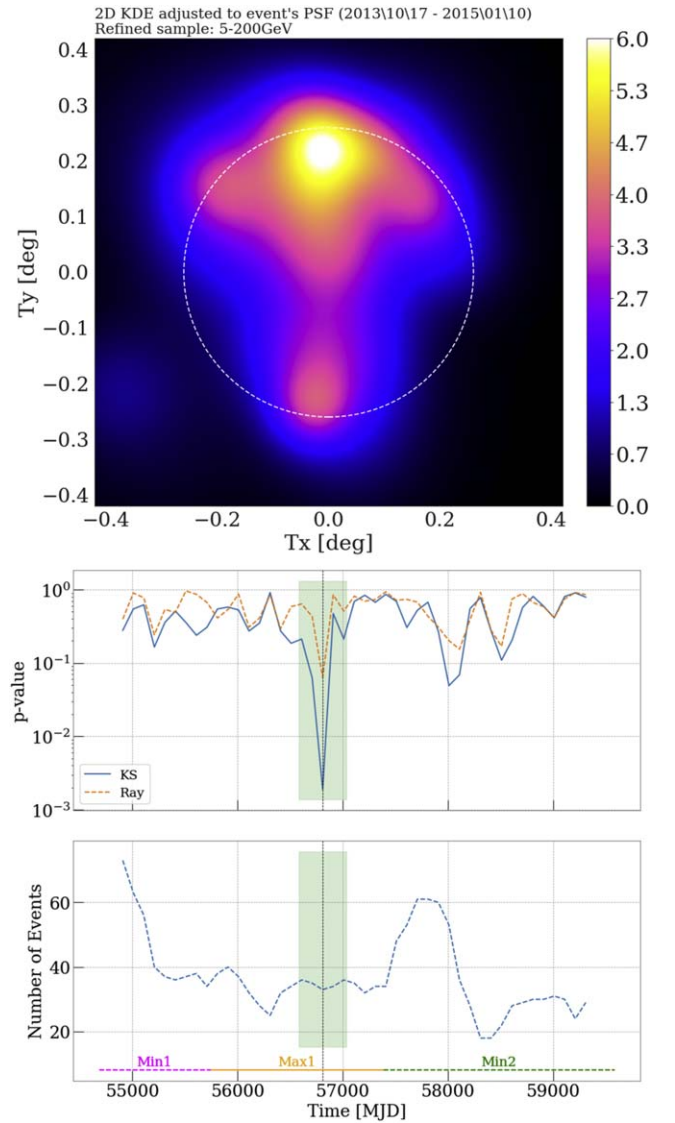


**Figure 8.** This figure presents diagnostic plots (i) and (vi) for the entire sample (top and bottom panels, respectively), which includes events with energies ranging from 5 to 150 GeV. In this case, the diagnostic plots are derived from a time window centered on MJD 56807.6, integrating data across a span of 450 days, from 2013 October 17 to 2015 January 10. This frame represents a period with the lowest  $p$ -values for the KS test, which coincided with the polar magnetic field flip at the maximum of cycle’s 24 solar activity.

to unveil the unidirectional excess to the north and south, respectively. Therefore, we note that the KS test demonstrated reliable sensitivity to unveil the presence of bipolar emission patterns aligned to the rotation axis. In this test, the anisotropic signature revealed by the KS test does not depend on the energy sampling and reinforces the robustness of our detection.

For a more detailed visual inspection of the events distribution evolving over time, we refer the reader to the corresponding animations in the online supplementary material, associated to Figures 6 and 7.

## 7. Conclusions

In this study, we investigated the properties of the solar disk  $\gamma$ -ray emission, with data obtained from the Fermi-LAT satellite over 2008 August to 2022 January. Our analysis shows robust evidence indicating anisotropic and energy-

dependent asymmetries, offering valuable insights into its nature and extending Orlando & Strong (2008), Ng et al. (2016), and Linden et al.’s (2018, 2022) pioneering works.

To ensure the reliability of our  $\gamma$ -ray sample, we have applied a series of comprehensive data cuts that systematically exclude times when the solar path is linked to known and potential contaminants. This includes the solar transit through the galactic-disk background and close encounters with the Moon. It also includes coincidences with GRBs, transits associated with known  $\gamma$ -ray sources (4FGL-DR3, 2FAV, 1FLT, and 2BIGB), as well as transits regarding blazars and blazar candidates in general (even for those not yet detected in  $\gamma$ -rays).

The initial phase of our analysis focuses on a careful examination of the GeV  $\gamma$ -ray distribution over the solar disk, evaluating its relation to energy and solar cycles. To that end, we consider  $\gamma$ -ray events within the following solar activity cycles: Min1, Max1, and Min2. We combine both KS and Rayleigh tests to investigate the existence of anisotropic trends and energy dependencies within each cycle. With this approach, we found relevant anisotropic trends in  $\gamma$ -ray emissions, most notably at the Max1 50 GeV channel, with excess counts toward the solar south pole. We also recover a significant anisotropic trend at the 9 GeV energy bin for the Min1p2 sample (a combination of Min1 and Min2 samples), revealing compelling evidence of anisotropic and energy-dependent trends in the solar disk  $\gamma$ -ray emission. Through this initial analysis, we demonstrate that a combination of the KS and Rayleigh tests provides a powerful tool to investigate the solar disk emission across different time windows and energy bins.

In the subsequent phase of our study, we divided our sample into lower (5–20 GeV) and higher (20–150 GeV) energy events. Our aim was to investigate energy-dependent features over time, which we achieved by integrating the  $\gamma$ -ray events over a moving time window and storing the results as frames. This strategy enabled us to build a dynamic visualization of the  $\gamma$ -ray distribution over time, essentially an animation of our data exploration. This approach yielded a unique perspective on the temporal evolution of the observed anisotropies.

Through our visualization we were able to pinpoint the most prominent anisotropic signatures in both low- and high-energy samples, which emerged around MJD 56820 (approximately 2014 June).

This period shows an intriguing dipole-like pattern, which is energy dependent and coincident with the polar magnetic field flip during the cycle 24 solar maximum. This observation reinforces the idea of a potential link between  $\gamma$ -ray emission, the solar magnetic configuration, and solar cycles. Our analysis estimates a  $3.7\sigma$  association between the asymmetric  $\gamma$ -ray emission and the polar magnetic field flip at the cycle 24 solar maximum. Looking ahead, we anticipate that the Fermi-LAT coverage of the ongoing Max2 cycle (from January 2022 onwards) will clarify whether the dipole pattern is typical of the solar maximum.

Our study presents a step forward in understanding solar  $\gamma$ -ray emissions and introduces new questions in the emerging field of Very High Energy Solar Astrophysics. We are likely observing the complex interplay of solar magnetic fields, solar atmospheric conditions, and incoming CRs, which includes fluctuations in CR flux and composition. There is a vast

scientific potential to exploring the physical processes that shape and influence the energy channels through which  $\gamma$ -rays are more likely to escape the solar surface. Based on our findings, we envisage that future  $\gamma$ -ray missions could benefit from the ability to provide real-time data on solar  $\gamma$ -ray activity, serving as an extra ingredient for solar forecasting models.

### Acknowledgments

We thank ApJ’s anonymous referee for the careful review and insightful comments. We acknowledge Melissa Pesce-Rollins, Philippe Bruel, Matthew Kerr, and especially Francesco Loparco for useful comments at the late stage of the manuscript. B.A. thanks the University of Trieste and the INFN—IT for the “Assegno di Ricerca” grant (2021 July to 2022 June) that supported the initial stages of this research, under the ASI-INAFF-CUP F82F17000240005 research project “Gamma rays from the Quiet Sun and Diffuse Emissions.” Further thanks go to the Institute of Astrophysics and Space Sciences (IA), University of Lisbon. B.A. is currently a Marie Skłodowska-Curie Postdoctoral Fellow at IA, funded by the European Union’s Horizon 2020 research and innovation program under the MSCA agreement No. 101066981. B.A. thanks the support from “Fundação para a Ciência e a Tecnologia” (FCT) through the research grant UIDP/04434/2020 (doi: [10.54499/UIDP/04434/2020](https://doi.org/10.54499/UIDP/04434/2020)). E.O. acknowledges the NASA grant No. 80NSSC20K1558. We acknowledge the *Centro de Computação* John David Rogers (CCJDR) at IFGW Unicamp, Campinas-Brazil, for providing access to the Feynman and Planck HPC Clusters, essential for the parallel computation of  $\gamma$ -ray light curves using the Fermi Science Tools. Additionally, part of this work utilizes archival data, software, or online services from the Space Science Data Center—ASI. The Fermi LAT Collaboration acknowledges generous ongoing support from a number of agencies and institutes that have supported both the development and the operation of the LAT and scientific data analysis. These include the National Aeronautics and Space Administration and the Department of Energy in the United States, the Commissariat à l’Énergie Atomique and the Centre National de la Recherche Scientifique / Institut National de Physique Nucléaire et de Physique des Particules in France, the Agenzia Spaziale Italiana and the Istituto Nazionale di Fisica Nucleare in Italy, the Ministry of Education, Culture, Sports, Science and Technology (MEXT), High Energy Accelerator Research Organization (KEK) and Japan Aerospace Exploration Agency (JAXA) in Japan, and the K. A. Wallenberg Foundation, the Swedish Research Council and the Swedish National Space Board in Sweden. Additional support for science analysis during the operations phase is gratefully acknowledged from the Istituto Nazionale di Astrofisica in Italy and the Centre National d’Études Spatiales in France. This work performed in part under DOE Contract DE-AC02-76SF00515.

*Facilities:* Fermi, SDO.

*Software:* astropy (Astropy Collaboration et al. 2013, 2018, 2022), sunpy (Mumford et al. 2020; The SunPy Community et al. 2020), scikit-learn (Pedregosa et al. 2011), scipy (Virtanen et al. 2020) fermi-sciencetools (Fermi Science Support Development Team 2019).

### ORCID iDs

Bruno Arsioli  <https://orcid.org/0000-0001-8166-6602>

## References

- Abdo, A. A., Ackermann, M., Ajello, M., et al. 2011, *ApJ*, 734, 116
- Abdollahi, S., Acero, F., Baldini, L., et al. 2022, *ApJS*, 260, 53
- Abdollahi, S., Ackermann, M., Ajello, M., et al. 2017, *ApJ*, 846, 34
- Ackermann, M., Ajello, M., Albert, A., et al. 2016, *PhRvD*, 93, 082001
- Agostinelli, S., Allison, J., Amako, K., et al. 2003, *NIMPA*, 506, 250
- Ajello, M., Angioni, R., Axelsson, M., et al. 2020, *ApJ*, 892, 105
- Ajello, M., Atwood, W. B., Baldini, L., et al. 2017, *ApJS*, 232, 18
- Ajello, M., Baldini, L., Bastieri, D., et al. 2021, *ApJS*, 252, 13
- Albert, A., Alfaro, R., Alvarez, C., et al. 2023, *PhRvL*, 131, 051201
- Albert, A., Alfaro, R., Alvarez, C., et al. 2018, *PhRvD*, 98, 123011
- Allen, C. W. 1951, *Obs*, 71, 157
- Altschuler, M. D., & Newkirk, G. 1969, *SoPh*, 9, 131
- Arsioli, B., & Chang, Y. L. 2017, *A&A*, 598, A134
- Arsioli, B., Chang, Y. L., & Musiimenta, B. 2020, *MNRAS*, 493, 2438
- Arsioli, B., Fraga, B., Giommi, P., Padovani, P., & Marrese, P. M. 2015, *A&A*, 579, A34
- Arsioli, B., & Polenta, B. 2018, *A&A*, 616, A20
- Astropy Collaboration, Price-Whelan, A. M., Lim, P. L., et al. 2022, *ApJ*, 935, 167
- Astropy Collaboration, Price-Whelan, A. M., Sipőcz, B. M., et al. 2018, *AJ*, 156, 123
- Astropy Collaboration, Robitaille, T. P., Tollerud, E. J., et al. 2013, *A&A*, 558, A33
- Atwood, W., Albert, A., Baldini, L., et al. 2013, arXiv:1303.3514
- Atwood, W. B., Abdo, A. A., Ackermann, M., et al. 2009, *ApJ*, 697, 1071
- Baldini, L., Ballet, J., Bastieri, D., et al. 2021, *ApJS*, 256, 13
- Banik, P., Bhadra, A., & Ghosh, S. K. 2023, arXiv:2305.17086
- Berens, P. 2009, *J. Stat. Softw.*, 31, 1
- Böhlen, T. T., Cerutti, F., Chin, M. P. W., et al. 2014, *NDS*, 120, 211
- Bonferroni, C. 1936, *Teoria Statistica Delle Classi e Calcolo Delle Probabilità* (Florence: R. Istituto Superiore di Scienze Economiche e Commerciali di Firenze)
- Brazier, K. T. S. 1994, *MNRAS*, 268, 709
- Cao, Z., della Volpe, D., Liu, S., et al. 2019, arXiv:1905.02773
- Chang, Y. L., Arsioli, B., Giommi, P., & Padovani, P. 2017, *A&A*, 598, A17
- Chang, Y. L., Arsioli, B., Giommi, P., Padovani, P., & Brandt, C. H. 2019, *A&A*, 632, A77
- Chupp, E. L., Forrest, D. J., Higbie, P. R., et al. 1973, *Natur*, 241, 333
- Darling, D. A. 1957, *Ann. Math. Stat.*, 28, 823
- De Angelis, A., Tatischeff, V., Tavani, M., et al. 2017, *ExA*, 44, 25
- Fermi Science Support Development Team, 2019 *Fermitools: Fermi Science Tools*, Astrophysics Source Code Library, ascl:1905.011
- Ferrari, A., Sala, P. R., Fasso, A., & Ranft, J. 2005, Technical Report SLAC-R-773, OSTI, doi: 10.2172/877507
- Fisher, N. I. 1996, *Statistical Analysis Of Circular Data* (Cambridge, UK: Cambridge Univ. Press), 277
- Fisher, R. 1953, *RSPSA*, 217, 295
- Fränz, M., & Harper, D. 2002, *P&SS*, 50, 217
- Gehrels, N., Chipman, E., & Kniffen, D. A. 1993, *A&AS*, 97, 5
- Glogowski, K., Bobra, M. G., Choudhary, N., Amezcua, A. B., & Mumford, S. J. 2019, *JOSS*, 4, 1614
- Gudiksen, B. V., Carlsson, M., Hansteen, V. H., et al. 2011, *A&A*, 531, A154
- Hochberg, Y. 1988, *Biometrika*, 75, 800
- Huentemeyer, P., BenZvi, S., Dingus, B., et al. 2019, *BAAS*, 51, 109
- Ishikawa, S.-n., Glesener, L., Christe, S., et al. 2014, *PASJ*, 66, S15
- Janardhan, P., Fujiki, K., Ingale, M., Bisoi, S. K., & Rout, D. 2018, *A&A*, 618, A148
- Johannesson, G., & Orlando, E. 2013, 33rd Int. Cosmic Ray Conf. (ICRC2013), 33 (Trieste: SISSA), 3106
- Kanbach, G., Bertsch, D. L., Fichtel, C. E., et al. 1993, *A&AS*, 97, 349
- Li, J.-T., Beacom, J. F., Griffith, S., & Peter, A. H. G. 2024, *ApJ*, 961, 167
- Li, Z., Ng, K. C. Y., Chen, S., Nan, Y., & He, H. 2020, arXiv:2009.03888
- Linden, T., Beacom, J. F., Peter, A. H. G., et al. 2022, *PhRvD*, 105, 063013
- Linden, T., Zhou, B., Beacom, J. F., et al. 2018, *PhRvL*, 121, 131103
- Masetti, N., Sbarufatti, B., Parisi, P., et al. 2013, *A&A*, 559, A58
- Massaro, E., Maselli, A., Leto, C., et al. 2015, *Ap&SS*, 357, 75
- Massey, F. J. 1951, *J Am Stat Assoc*, 46, 68
- Mazziotta, M. N., De La Torre Luque, P., Di Venere, L., et al. 2020, *PhRvD*, 101, 083011
- McEnery, J. E. 2017, AAS/HEAD Meeting 16, 103.13
- Moskalenko, I. V., & Porter, T. A. 2007, *ApJ*, 670, 1467
- Mumford, S., Freij, N., Christe, S., et al. 2020, *JOSS*, 5, 1832
- Ng, K. C. Y., Beacom, J. F., Peter, A. H. G., & Rott, C. 2016, *PhRvD*, 94, 023004
- Orlando, E. 2009, arXiv:0907.0557
- Orlando, E., Bottacini, E., Moiseev, A. A., et al. 2022, *JCAP*, 2022, 036
- Orlando, E., Petrosian, V., & Strong, A. 2023, *ApJ*, 943, 173
- Orlando, E., & Strong, A. 2007, *Ap&SS*, 309, 359
- Orlando, E., & Strong, A. 2021, *JCAP*, 04, 004
- Orlando, E., & Strong, A. W. 2008, *A&A*, 480, 847
- Parker, E. N. 1965, *P&SS*, 13, 9
- Pedregosa, F., Varoquaux, G., Gramfort, A., et al. 2011, *JMLR*, 12, 2825
- Petrie, G. J. D., Petrovay, K., & Schatten, K. 2014, *SSRv*, 186, 325
- Schatten, K. H., Wilcox, J. M., & Ness, N. F. 1969, *SoPh*, 6, 442
- Seckel, D., Stanev, T., & Gaisser, T. K. 1991, *ApJ*, 382, 652
- Share, G. H., Murphy, R. J., Tolbert, A. K., et al. 2018, *ApJ*, 869, 182
- Tang, Q.-W., Ng, K. C. Y., Linden, T., et al. 2018, *PhRvD*, 98, 063019
- The SunPy Community, Barnes, W. T., Bobra, M. G., et al. 2020, *ApJ*, 890, 68
- Thompson, D. J., Bertsch, D. L., Morris, D. J., & Mukherjee, R. 1997, *JGR*, 102, 14735
- Upton, L. A., & Hathaway, D. H. 2023, *JGRA*, 128, e2023JA031681
- Virtanen, P., Gommers, R., Oliphant, T. E., et al. 2020, *NatMe*, 17, 261
- von Kienlin, A., Meegan, C. A., Paciasas, W. S., et al. 2020, *ApJ*, 893, 46
- Zhou, B., Ng, K. C. Y., Beacom, J. F., & Peter, A. H. G. 2017, *PhRvD*, 96, 023015